



Solidification of Be-free Ni-based dental alloy

Franc ZUPANIČ¹, Carlos A. NUNES², Gilberto C. COELHO², Paula L. CURY², Gorazd LOJEN¹, Tonica BONČINA¹

1. Faculty of Mechanical Engineering, University of Maribor, 2000 Maribor, Slovenia;

2. Department of Materials Engineering, School of Engineering,
University of Sao Paulo, 12602-810 Lorena, Sao Paulo, Brazil

Received 1 November 2017; accepted 24 April 2018

Abstract: A novel, Nb- and Si-rich and Be-free Ni-based alloy was cast by two methods of investment casting and continuous casting to study the microstructure evolution during solidification and its mechanical properties. The solidification of the alloy started with the primary crystallization of FCC- γ , followed by a binary eutectic reaction, with the formation of a heterogeneous constituent: FCC- γ +G-phase, which replaced the low-melting eutectic (FCC- γ +NiBe) in the Be-bearing alloys. AlNi₆Si₃ and γ' formed during the terminal stages of solidification by investment casting, while the formation of AlNi₆Si₃ was suppressed by continuous casting. The Scheil solidification model agreed very well with the experimental results.

Key words: solidification; nickel alloy; continuous casting; investment casting; microstructure; dental alloy

1 Introduction

The nickel-based dental alloys are commonly used as a substructure of metal–ceramic crowns. The main advantages of their usage are much lower price, increased modulus of elasticity, and higher strength compared with gold. Thus, thinner sections of the alloy can be used and, consequently, tooth destruction during the crown preparation is less probable. Additionally, the metal and ceramic crowns can be bonded intimately during firing, because the thermal expansion coefficient of Ni-based alloys is well matched to that of the conventional porcelain [1]. On the other hand, the corrosion resistance of these alloys somewhat limits their usage and triggers the development of new metallic alloys for dental applications [2]. Nickel-containing dental alloys can initiate some health problems [3]. However, when they are used according to established techniques, they do not pose a risk to patients or members of the dental team [4]. Thus, it could be expected that Ni-based alloys will remain widely used as a substitute for much more expensive precious metal alloys in the next years.

Ni-based dental alloys are produced mainly by vacuum induction melting, followed by the investment casting of rods, which are eventually cut to sizes

appropriate for work in dental laboratories. The continuous casting of Ni-based superalloys was developed less than 20 years ago [5], and today represents an established method for providing high-quality alloys for the automotive and aerospace industries. There have been no corresponding reports in the scientific literature regarding the continuous casting of Ni-based dental alloys. Thus, the first goal of our study was to manufacture a Ni-dental alloy by continuous casting. In this way, one could produce alloys with significant advantages over the traditional manufacturing methods. Namely, the products can be extremely clean and almost free of oxides and other harmful inclusions. Due to higher cooling rates, their microstructures are finer, providing better uniformity, higher mechanical properties, and shorter melting time, due to smaller intermetallic phases. Further benefits of continuously cast dental alloys include the improved surface finish, which eliminates the need for grinding, the absence of centreline porosity, and the reduced waste when cutting to weight.

By the selection of the appropriate alloy, we took into account the work of ALKMIN et al [6], who investigated several Be-containing and Be-free Ni-based dental alloys. The role of beryllium in these alloys is to decrease the liquidus and solidus temperatures and improve the castability. In fact, the recent investigation

has shown that beryllium does not irritate skin and eyes, and does not induce any clinical signs of acute oral toxicity [7]. Nevertheless, these alloys are more susceptible to localized corrosion attack due to the presence of an intermetallic NiBe phase in the eutectic structure [8]. Thus, a Ni–Cr–Mo alloy without Be and rich in Nb and Si was selected for further studies. This alloy exhibited passive corrosion behavior in artificial saliva and mouthwash solutions, and the cytotoxicity assay indicated that the alloy was not cytotoxic in the negative control when using a titanium plate [6].

The main goal of this investigation was to determine the solidification sequence during investment and continuous casting processes by a combination of experiments and computational thermodynamics. This has not yet been reported for the Nb- and Si-rich Ni-based alloys that do not contain Be. The behavior of continuously cast samples by compression tests was also studied to investigate the possibility of the alloy for other applications apart from dentistry.

2 Experimental

The alloy was produced by vacuum induction melting (VIM) using commercially available alloying elements. The melting and homogenization lasted between 10 and 15 min. The investment cast bars with a diameter of 25 mm were produced by casting into ceramic shells preheated to 200 °C. The pouring temperatures were between 1515 and 1575 °C.

The alloy was cast continuously by using a pilot-scale set up consisting of a Leybold Heraeus vacuum induction melting furnace and a Technica Guss vertical continuous caster. The vertical continuous caster can pull rods with diameters from 5 to 16 mm out of the mould. It is described in greater detail in Ref. [9]. Approximately 10 kg of the investment cast bars were melted under a vacuum of 0.1–1 Pa in an alumina crucible. A protective argon atmosphere was used during continuous casting. The temperature of the melt at the beginning of casting was approximately 100 °C above the alloy's liquidus temperature. The alloy solidified within a water-cooled copper-alloy mould (diameter 10 mm). The rod was extracted using an “alternating drawing mode” consisting of the drawing stroke and the resting period. The average casting speed was 520 mm/min. The chemical composition of the alloy is given in Table 1.

Light microscopy (LM) work was done using a Nikon Epiphot 300. Samples were prepared using conventional mechanical grinding and polishing and etched by an etchant consisting of 37 mL HCl, 6.3 g K₂Cr₂O₇ and 125 mL distilled water. The scanning electron microscopy (SEM) was carried out in an FEI™

SIRION NC and FEI™ Quanta 3D, and the transmission electron microscopy (TEM) was carried out in an FEI™ Tecnai F20. The TEM specimen was cut out using a focused ion beam (FIB) in an FEI™ Nova 200. X-ray diffraction (XRD) with Cu K_α radiation was carried out between 2θ values of 30° and 118°, with a step of 0.02° and holding time of 1 s, using a PANalytical Empyrean diffractometer. Minor phases in the investment cast sample (e.g. the G-phase and AlNi₆Si₃) were extracted by electrochemical dissolution of the matrix in a solution of 40 mL HCl and 4 g tartaric acid in 360 mL methanol at 3 V. Differential thermal analysis (DTA) was done in the temperature range of 30–1350 °C, with heating and cooling rates of 10 °C/min in an alumina crucible using Netsch STA 449 F3. The Vickers hardness of HV 30 was measured using Buehler Micromet 2004. The compression tests of 11 continuously cast specimens with a diameter of 3 mm and a height of 6 mm were carried out using EMIC DC10000, at a rate of 0.5 mm/min and room temperature.

Thermodynamic calculations were carried out using PANDAT software and the TT-Ni8 database.

Table 1 Chemical composition of alloy determined by X-ray fluorescence (XRF, PANalytical Axios MAX) and content of carbon determined according to ASTM E1019 (Leco CS744) (mass fraction, %)

Cr	Mo	Si	Ti	Al
9.29	2.46	3.68	0.38	2.0
Nb	C	B	Be	Ni
3.38	0.002	<0.001	<0.001	Rest

3 Results and discussion

3.1 Microstructure

Figure 1 shows the micrographs of the investment cast and continuously cast samples. The microstructures consisted of the dendritic FCC-γ matrix, with some other phases in the interdendritic regions. The investment cast sample contained mainly equiaxed grains with dendritic morphology. The average secondary dendrite arm spacing was (70±10) μm, which was only slightly smaller on the surface than that at the casting centre. On the other hand, in the continuously cast sample, columnar grains prevailed, with the average secondary dendritic arm spacing of (6±1) μm. The difference between both specimens arises from the unequal cooling rates. The estimated cooling rate for the similar casting shapes and casting methods was around 1 °C/s for the investment cast sample [10]. The cooling rate close to the surface was 100–150 °C/s, and the temperature in the centre of the continuously cast rod was 20–30 °C.

Different cooling rates not only caused the variations in the fineness of the microstructure but also

influenced the phase compositions strongly, which was revealed by XRD. Figure 2 shows the comparison of XRD patterns of the investment and continuously cast samples. Both samples contained the Ni-based solid

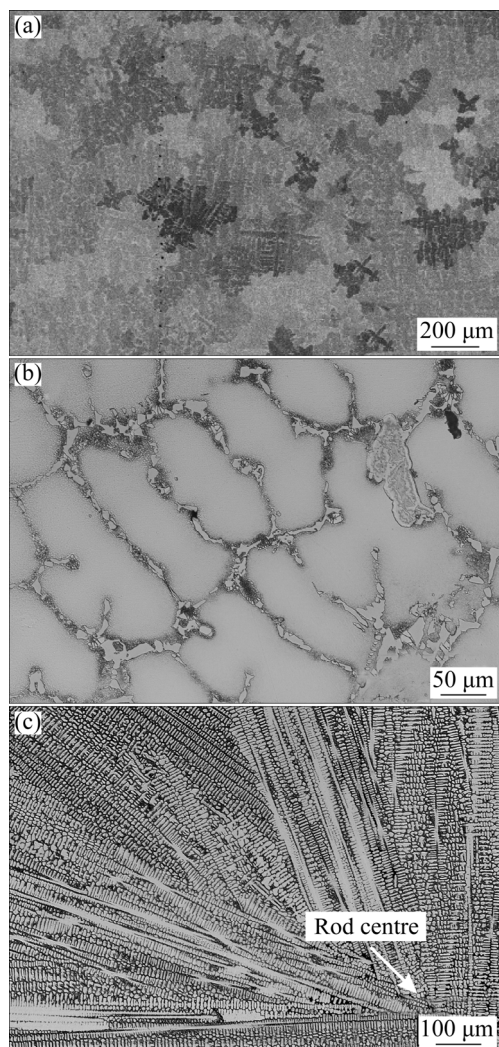


Fig. 1 Light optical micrographs of investigated alloy: (a, b) Investment cast sample; (c) Continuously cast sample

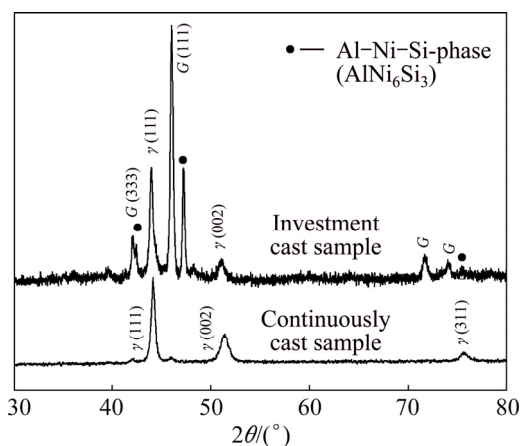


Fig. 2 XRD patterns of bulk continuously cast sample and extracted particles of investment cast sample

solution (γ) with an FCC-structure. The lattice parameters in both samples differed only slightly (continuous cast sample: $a=(0.3571\pm 0.0001)$ nm, investment cast sample: $a=(0.3572\pm 0.0330)$ nm).

The FCC- γ phase represented the major dendritic structure in both samples (Fig. 1). The peaks of γ' -L1₂, e.g. {100} and {110}, cannot be discerned in Fig. 1. However, a detailed investigation of the XRD pattern revealed their presence. Other peaks of γ' -L1₂ coincided with that of the γ -phase, due to the very similar lattice parameters of both phases. Thus, the dendrites were composed of the γ matrix and γ' precipitates. The presence of Al and Ti enabled the formation of a γ' -L1₂ phase. In the continuously cast sample, much smaller peaks could also be seen in the XRD pattern. Considerably higher peaks also existed at the same positions in the XRD pattern of the investment cast sample. The peaks coincided entirely with the peaks of the G-phase [11]. The G-phase has a nominal chemical formula of Ni₁₆Nb₆Si₇. It has frequently been found in stainless steels containing Si and Nb [12,13]. The G-phase also has an FCC-structure, with the lattice parameter $a=(1.1197\pm 0.0009)$ nm in the investment cast sample, and $a=(1.1194\pm 0.0022)$ nm in the continuously cast sample, which is much larger than that of the FCC- γ . The XRD pattern of the investment cast sample also had additional peaks that were not present in the XRD pattern of the continuously cast sample. Some peaks coincided nicely with the peak positions of the phase AlNi₆Si₃ [11], which is also included in the powder diffraction files (PDF 00–49–1448). It is supposed to be an Al-solid solution of θ -Ni₂Si phase arising from the binary Ni–Si system. The lattice parameters of the hexagonal AlNi₆Si₃ were $a=(0.7710\pm 0.0012)$ nm, and $c=(1.4757\pm 0.0002)$ nm.

These results showed that FCC- γ , L1₂- γ' and G-phase were present in both samples, and that the phase AlNi₆Si₃ appeared additionally in the investment cast sample. The solidification obviously started in both samples with the primary crystallization of FCC- γ , and other phases formed in the interdendritic region during the final stages of solidification, while most of the L1₂- γ' formed during precipitation in the solid state.

3.1.1 Detailed microstructure of investment cast sample

Figure 3(a) shows a backscattered electron micrograph of the investment cast sample, revealing much more detail than the micrographs in Fig. 1. The phases revealed by the XRD are indicated in the micrograph. The dendrites, which were, in fact, a two-phase mixture consisting of FCC- γ and precipitates L1₂- γ' that formed upon continuous precipitation during cooling, represented the major volume fraction. Microsegregation occurred during the growth of the dendrites. The contents of Al, Si, Ti and Nb increased,

while the contents of Mo and Cr decreased from the dendrite centers towards their edges. A similar behavior was also found in other Ni-alloys [14].

The size and volume fraction of precipitates rose from dendrite arm centers towards the interdendritic regions, and their shape changed from the cubes in the dendrite centers towards octodically diced cubes, and even to octodendrites (Fig. 3(b)), according to the definition of $L1_2$ - γ' shapes in Ref. [15]. During precipitation, redistribution of the alloying elements also took place. The qualitative EDS analyses revealed that the precipitates were enriched by Al, Ti, Si and Nb, and depleted by Cr and Mo. Al, Ti, Si and Nb, namely, can all be present in the $Ni_3(Al, Ti, Si, Nb)$ phase [16].

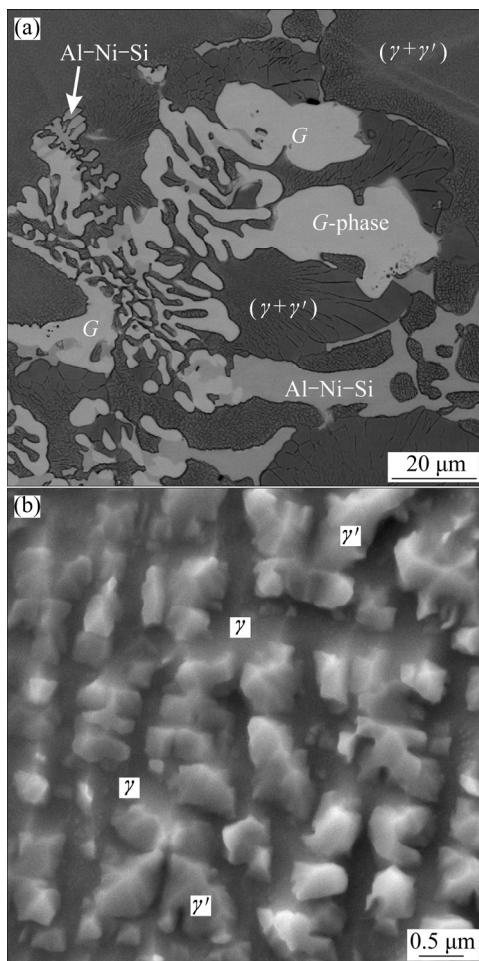


Fig. 3 Backscattered electron micrographs of investment cast sample: (a) Interdendritic regions; (b) Precipitates at edge of FCC- γ dendrite

All phases detected by XRD were found in the interdendritic regions. At least five EDS analyses were carried out in each phase and each area. The homogeneous areas of the G -phase and $AlNi_6Si_3$ phase were large enough to obtain the reliable and reproducible results. By analysis of the γ' phase in the two-phase ($\gamma+\gamma'$) region and $AlNi_6Si_3$, the results largely scattered, because the electron interaction volume probably

exceeded the size of the individual analysed particles at 10 kV of accelerating voltage. The results of the EDS analyses are shown in Table 2. It was evident that the G -phase contained not only Nb, Ni and Si as its chemical formula suggests, but also 11.0% Mo and 7.0% Cr. This phase belonged to a structure type of $Mg_6Cu_{16}Si_7$, which allowed the substitution of the atoms on different sublattices [11]. The same applies to the phase with the nominal composition of $AlNi_6Si_3$, which also contained Cr and Nb. The content of Ni was rather high, which indicated that interaction volume exceeded the size of the investigated particles.

Table 2 Chemical compositions of phases in investment cast (IC) and continuously cast (CC) samples determined using EDS accelerating voltage of at 10 kV (mole fraction, %)

Resource	Al	Si	Ti	Cr	Ni	Nb	Mo
Dendrite centre (IC)	4.8	7.4	0.4	11.6	71.9	2.0	1.9
Standard deviation	0.1	0.1	0.1	0.3	0.3	0.1	0.2
Dendrite edge (IC)	6.4	9.4	0.7	7.40	72.5	2.6	1.0
Standard deviation	0.2	0.2	0.1	0.2	0.4	0.1	0.2
$(\gamma+\gamma')$ (IC)	7.0	11.4	0.9	4.5	73.3	2.5	0.4
Standard deviation	0.2	0.3	0.1	0.2	0.5	0.2	0.1
Individual γ' (IC)	7.89	12.05	0.91	3.45	73.30	2.40	0.01
Standard deviation	0.2	0.2	0.1	0.3	0.4	0.1	0.2
$AlNi_6Si_3$ (IC)	6.7	12.7	0.8	3.3	73.9	2.4	0.2
Standard deviation	1.0	1.9	0.1	0.1	0.7	0.4	0.1
G -phase (IC)	0.2	18.6	0.3	7.0	49.69	13.3	11.0
Standard deviation	0.17	0.12	0.07	0.27	0.44	0.19	0.83
Dendrite (CC)	5.0	5.4	0.3	11.8	74.1	1.5	1.9
Standard deviation	0.1	0.5	0.1	0.1	0.5	0.1	0.2
Eutectic ($\gamma+G$) (CC)	0.7	10.7	0.7	5.5	64.3	14.6	3.5
Standard deviation	0.3	0.5	0.1	0.2	1.1	0.6	0.3

In the interdendritic regions, a two-phase constituent (FCC- $\gamma+L1_2$ - γ') was also always present. This two-phase constituent may have formed by the eutectic reaction during solidification. It contained more Al, Ti, Si and Nb and less Cr and Mo than the average composition of the alloy. The γ' contained more γ' -forming elements Al, Si, Ti and Nb than the average composition of the ($\gamma+\gamma'$) region (Table 2). Similar ($\gamma+\gamma'$) eutectic regions were found by MA and SAHM [17] in the superalloy SRR99. ZHAO et al [18] have found that the ($\gamma+\gamma'$) precipitation began with a peritectic reaction of $L+\gamma\rightarrow\gamma'$ and developed by the eutectic reaction of $L\rightarrow\gamma+\gamma'$.

3.1.2 Detailed microstructure of continuously cast sample

The crystal grains in the continuously cast sample grew with a typical dendritic morphology (Fig. 1(c)).

The distances between the primary and secondary arms increased slightly with increasing distance from the rod surface. In the longitudinal direction, the rods showed a periodic macrostructure, caused by the alternating drawing mode, similar as the case in Ref. [9]. The γ grains propagated almost perpendicularly to the rod surface during the drawing stroke, while they grew to the casting direction during the resting period. The secondary arm spacings were 5–7 μm on the surface and 6–8 μm at the centre.

Typical microstructures of continuously cast samples are shown in Figs. 4 and 5. The microstructure consisted of γ -dendrites and binary eutectic ($\gamma+G$ -phase). In the same area, an additional phase was revealed on the FIB-cross-section (indicated by the arrow in Fig. 5(b)), which might be the AlNi_6Si_3 phase found in the investment cast sample. Since its volume fraction was very low, it could be expected that its effect on properties was inferior, and which was the reason that has not been studied in detail. The morphology of the intermetallic eutectic G -phase was typical for a complex regular eutectic [19]. Close examination using TEM showed that the G -phase formed on the dendritic arms of γ , and then grew into the remaining liquid (Fig. 6(a)). The G -phase can branch rapidly, thus responding readily to variations in solidification conditions, and adapting to the available space in the interdendritic region. Typical sizes of the eutectic cells were a few micrometres, while the distances between the eutectic arms were a few tenths of a micrometre.

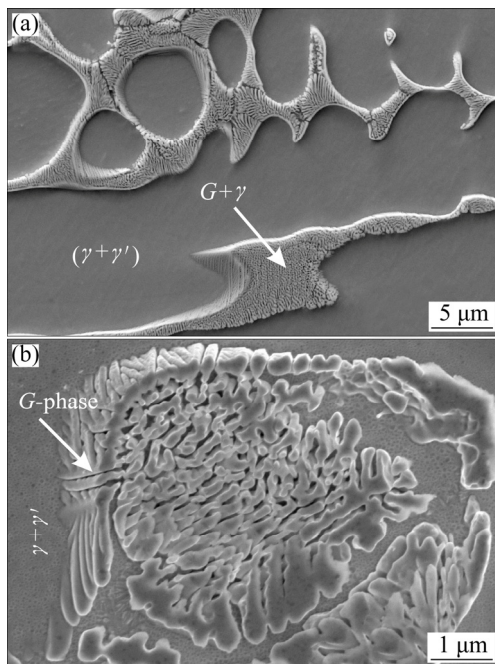


Fig. 4 Backscattered electron micrographs of continuously cast specimen along longitudinal cross-section: (a) Microstructure at rod centre; (b) Enlarged interdendritic spaces with binary eutectic (FCC- $\gamma+G$ -phase)

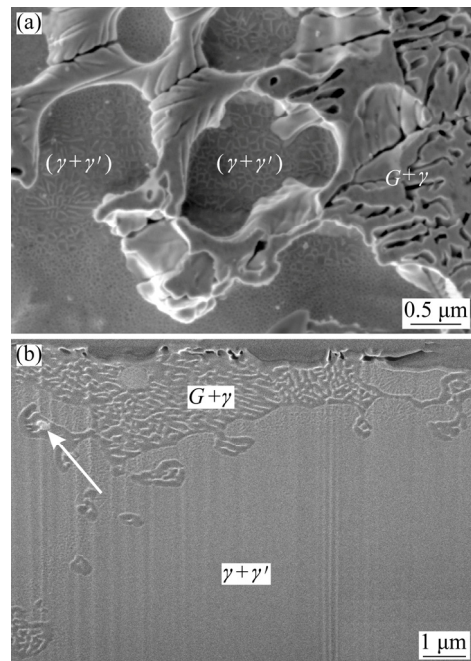


Fig. 5 Microstructures of continuously cast sample using FIB: (a) Ion-induced secondary electron image of metallographic cross-section; (b) Secondary ion image of FIB-cross-section

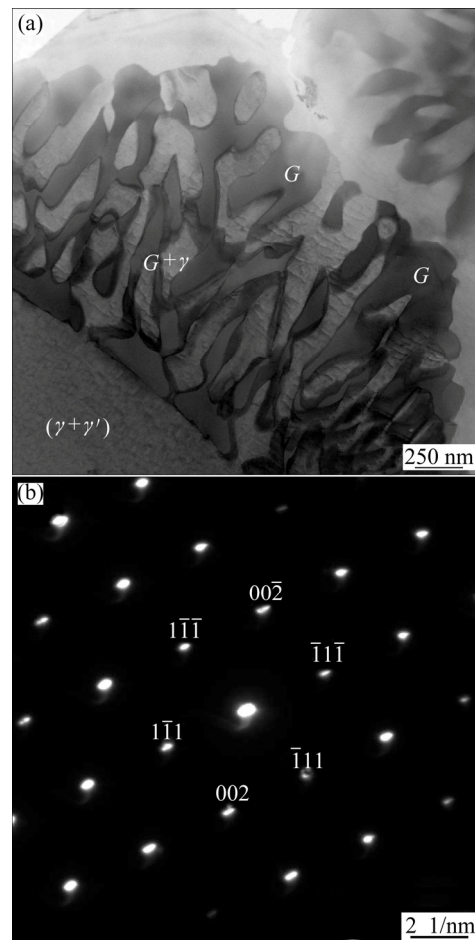


Fig. 6 TEM images of continuously cast rod: (a) Interdendritic space with binary eutectic; (b) Selected area diffraction pattern taken along $[110]$ axis of eutectic G -phase

Figure 6(b) shows the selected area diffraction pattern (SADP) taken along [101] axis of the FCC G -phase. From the positions of diffraction spots, the lattice spacing of G -phase was (1.129 ± 0.010) nm.

Figure 5(a) shows that, within the interdendritic regions, discontinuous precipitation of γ' could also be observed. The continuous precipitation of γ' took place elsewhere. Figure 7(a) shows TEM image of area close to dendrite center in continuously cast rod, indicating the Ni-solid solution γ , with γ' -precipitates. The volume fraction of the γ' -precipitates was much larger than that of the γ -phase, but lower than that in the most advanced superalloys [20]. Figure 7(b) proved that γ and γ' had almost the same lattice parameters and were coherent. The evaluated lattice parameters of both phases were: $a = (0.348 \pm 0.003)$ nm. The γ' -precipitates formed during cooling in the solid state, below the solvus temperature of alloy.

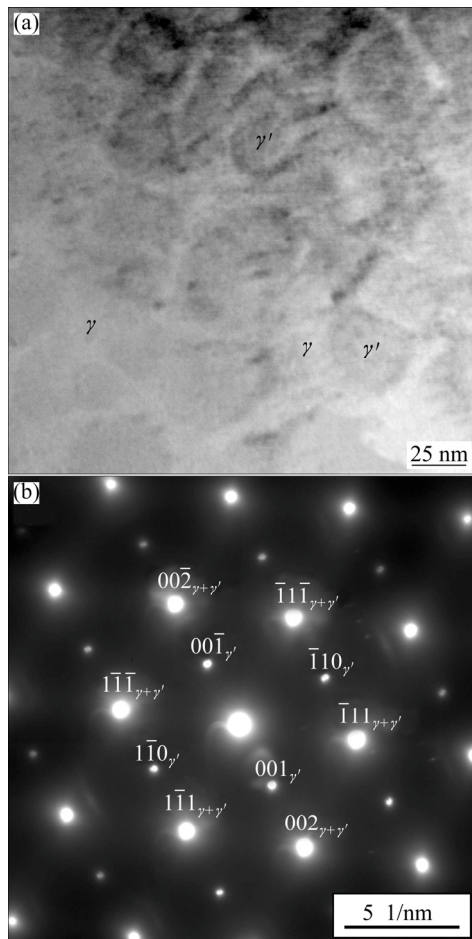


Fig. 7 TEM image of area close to dendrite centre in continuously cast rod: (a) Matrix ($\gamma+\gamma'$); (b) Selected area diffraction pattern

3.2 Mechanical properties

Dental alloys are used mainly in the as-cast condition. Thus, the properties in the as-cast state are the most important. However, this new alloy contains a small

fraction of coarse intermetallic compounds, which is more pronounced for the continuously cast sample. Thus, this alloy could have a good plasticity, which may lead to the application of the alloy in areas out of dentistry. Hardness measurement showed that the alloy in both conditions possessed a hardness of HV (450 ± 10) . This hardness is typical for the precipitation of the hardened Ni-based superalloy. ALKMIN et al [6] obtained the following tensile properties for the investment cast alloy: 0.2%-proof-stress (810 ± 25) MPa, tensile strength (845 ± 18) MPa, while the elongation at fracture only was 0.6%. Therefore, the investment cast alloy is not appropriate for forming. Thus, the continuous cast bars were selected for performing a compression test to gain information about the plastic behavior of the investigated alloy. Typical room-temperature curves for engineering stress versus true strain and true stress versus true strain are given in Fig. 8 for a continuously cast sample. The 0.2%-proof-stress was (1028 ± 78) MPa, and the maximum true stress was (1692 ± 70) MPa. The 0.2-proof stress was, thus, approximately 20% higher than that for the investment cast samples, which can be related to the finer microstructure of the continuously cast rods. The true deformation at fracture was between 0.09 and 0.15. At this deformation, the first cracks appeared in the samples. The continuously cast samples also showed considerable strain hardening. At only true strain of 0.1, the true stress increased by more than 600 MPa. These results showed that the continuously cast rods possessed rather good plasticity, even at room temperature. Thus, they could be shaped by different forming processes. Moreover, the properties are similar to those of several Ni-based superalloys (e.g. Astroloy, Inconel 706, Udimet 700) [21].

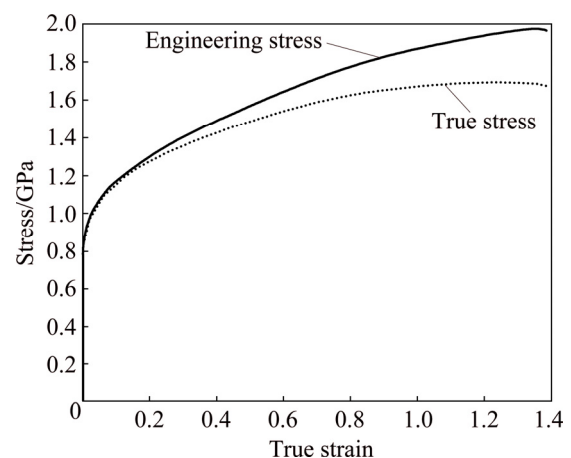


Fig. 8 Engineering and true stresses in plastic region of compression test for continuously cast sample

3.3 Computational thermodynamics

A thermodynamic modelling was carried out to obtain a better insight into the equilibrium phase

compositions of the investigated alloy. Figure 9 shows the calculated equilibrium phases and phase volume fractions as a function of temperature for the composition corresponding to the alloy in Table 1. The liquidus, solidus and gamma-prime solvus temperatures were 1312, 1240 and 1011 °C, respectively. Thus, under the equilibrium conditions, the solidification range was approximately 72 °C.

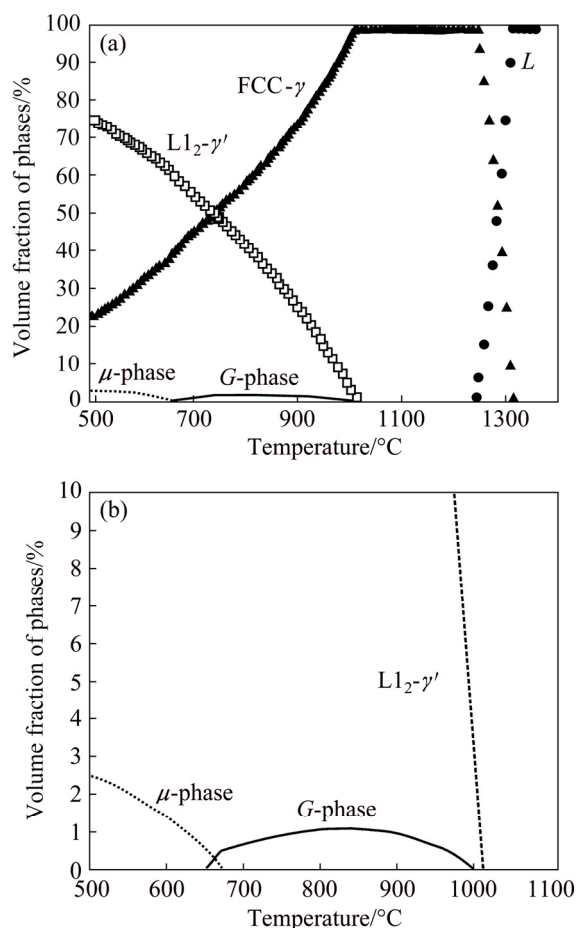


Fig. 9 Equilibrium phases in 78.7Ni–9.3Cr–2.5Mo–3.7Si–0.4Ti–2.0Al–3.4Nb alloy (mass fraction, %): (a) Calculated equilibrium phases and phase volume fraction between 500 and 1400 °C; (b) Enlarged region from 500 to 1100 °C showing volume fractions of minor phases

The equilibrium solidification would be, in fact, one-phase solidification, because only the γ -phase formed from the liquid. The γ' -phase precipitated from the γ -phase below the solvus temperature, and its volume fraction can be as high as 65% at 600 °C. Under the equilibrium conditions, the G -phase was formed in the solid state. It was thermodynamically stable between 650 and 1000 °C. Its formation was caused by a decrease of silicon solubility in the γ -phase. Further calculations showed that the G -phase should appear under equilibrium conditions when the alloy contained more than 3.5% silicon (mass fraction). Figure 9 also

suggested that, below 700 °C, the Laves μ -phase (based on Ni_2Nb intermetallic phase) might appear as a stable phase. This phase was not present in the microstructure. The phase with the nominal composition of $AlNi_6Si_3$, which was found in the investment cast sample, was not predicted as a stable phase (it was modelled as Ni_2Si phase that had large solubility ranges for several elements, including Al).

The segregation of alloying elements occurred during crystallization. Thus, the equilibrium solidification is not the most appropriate for the prediction of the solidification sequence. The segregation of alloying elements can be predicted by the solidification simulation according to the Scheil model [22,23]. The Scheil solidification model assumes the equilibrium conditions at the solid–liquid interface, complete mixing in the liquid phase, and the absence of diffusion in the solid state. The calculated volume fraction of the solid as a function of temperature is depicted in Fig. 10. It is clear that several phases can form from the liquid state, which is entirely different from the equilibrium conditions. Table 3 shows the temperature intervals and the reactions taking place during solidification. The temperature ranges are also indicated in Fig. 10. The solidification temperature interval under such conditions is 213 °C, which is much wider than under equilibrium conditions. The non-equilibrium conditions can cause different side effects.

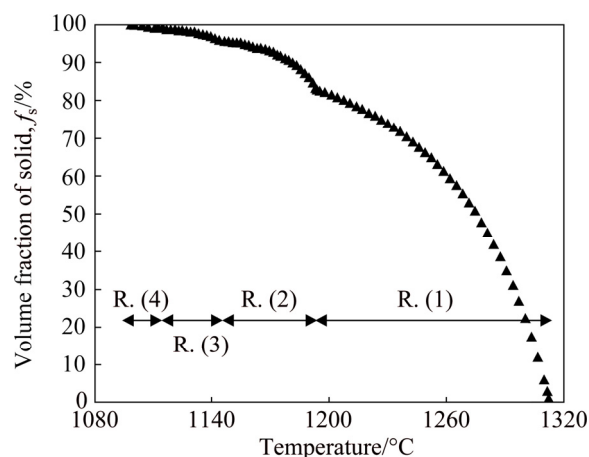


Fig. 10 Calculated volume fraction of solid according to Scheil solidification model

The solidification starts at 1312 °C with the primary precipitation of FCC- γ (Reaction (1)), which was the same as that predicted by the equilibrium calculations. The contents of Ni and Cr decreased from the core of the FCC- γ , while the contents of Si, Mo and Nb increased. The contents of Si, Nb and Mo increased in the remaining liquid, which led to the formation of the G -phase at 1193 °C, and to the binary eutectic reaction $L \rightarrow FCC-\gamma + G$ -phase (Reaction (2)). When the binary

eutectic reaction ceased at 1143 °C, the solid volume fraction was around 95%, and it consisted only of FCC- γ and the G -phase. By the solidification of the last 5% of the remaining liquid, minor fractions of the Laves μ -phase and γ' -phase formed according to Reactions (3) and (4). The solidification was finished at 1099 °C. The formation of Laves phase was also found in other nickel alloys [24]. Also, in this case, the phase with the nominal composition of AlNi_6Si_3 was not predicted to form during the solidification. The calculated volume fraction of G -phase (around 2%) was close to its volume fraction in the continuously cast sample. However, the calculations showed that the content of the G -phase almost corresponded to the stoichiometric composition ($\text{Nb}_6\text{Ni}_{16}\text{Si}_7$), while the experimental results indicated substantial solubility of Mo and Cr in it (Table 2).

3.4 Differential thermal analysis

Figure 11 shows the DTA heating and cooling curves. The starting condition was a sample after a controlled cooling with 10 °C/min. Its final microstructure was similar to that of the investment cast sample (Fig. 3(a)). On the heating curve, three endothermic peaks were observed, while on the cooling curves several peaks were present. The DTA-analysis showed quite wide solidification range. The liquidus temperature was approximately 1300 °C, and the solidus temperature (the incipient melting temperature) was 1100 °C. This result is close to the prediction of the solidification by the Scheil model.

The first peak by the cooling was related to the primary solidification of γ ($L \rightarrow \gamma$), which had an equivalent peak on the heating curve. The other peaks

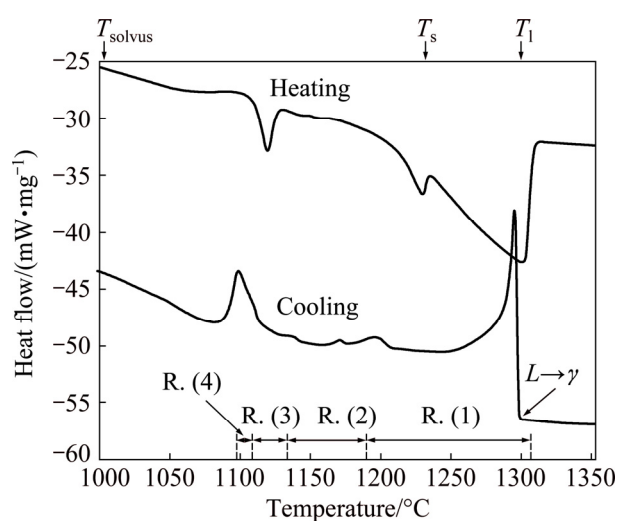


Fig. 11 DTA heating and cooling curves (T_l , T_s and T_{solvus} indicate calculated equilibrium liquidus, solidus and γ' -solidus temperatures, respectively; ranges of R. (1)–R. (4) indicate temperature ranges of reactions in Table 3, calculated by Scheil model)

were related to the reactions predicted by the Scheil model. The temperature regions for reactions taking place during solidification by the Scheil model (Table 3) are indicated in Fig. 11. They can reasonably explain the peaks on the cooling curve.

Table 3 Temperature ranges of reactions calculated by Scheil solidification model, and comparison with peak temperatures determined by DSC

Reaction code	Temperature range/°C	Temperature range in DSC (Fig. 11)/°C	Reaction
R. (1)	1312–1193	1302–1240	$L \rightarrow \text{FCC-}\gamma$
R. (2)	1193–1143	1210–1161	$L \rightarrow \text{FCC-}\gamma + G\text{-phase}$
R. (3)	1143–1113	1145–1129	$L \rightarrow \text{FCC-}\gamma + G\text{-phase} + \text{Laves}$
R. (4)	1113–1099	1125–1080	$L \rightarrow \text{FCC-}\gamma + G\text{-phase} + \text{Laves} + \text{L1}_2\text{-}\gamma'$

3.5 Microstructure evolution during solidification of investment cast and continuously cast samples

The solidification of Ni-based alloys normally started with the primary crystallization of FCC- γ . In polycrystalline alloys, C and B segregated into the remaining liquid, and during the final states of solidifications, ($\gamma + \text{MC}$) and ($\gamma + \text{M}_3\text{B}_2$) were formed. This was found in different alloys, such as IN 100 [25], IN 713C [5], GMR 235 [10], Nb-bearing superalloy [26] and several others. The eutectics ($\gamma + \text{Laves phases}$) [23,24,26,27] and ($\gamma + \gamma'$) also occurred in some alloys [17,18]. An eutectic (FCC- $\gamma + \text{NiBe}$) was formed in Be-bearing alloys [6,8].

According to the microstructural analysis, DTA and thermodynamic modelling, it is possible to explain rationally the microstructure evolution in the investment cast and continuously cast samples. The solidification range obtained by the Scheil model and DTA agreed very well. It amounted to more than 200 °C, which was much greater than the difference between the equilibrium liquidus and solidus temperatures (≈ 72 °C).

The primary solidification started by the formation and growth of FCC- γ dendrites, with simultaneous positive segregation of Al, Si, Ti, and Nb, and negative segregation of Cr and Mo. The enrichment of the remaining liquid led to the formation and growth of the binary eutectic (FCC- $\gamma + G$ -phase). This reaction was followed by the formation of the AlNi_6Si_3 -phase, which grew simultaneously with the FCC- γ and G -phase in the remaining liquid (Reaction 3). The formation of the AlNi_6Si_3 phase was almost completely suppressed in the continuously cast sample due to much higher cooling

rate. The supersaturation of the remaining liquid with Al and Ti led to Reaction 4. In fact, during this reaction, pockets of the remaining liquid transformed to apparently two-phase regions indicated by $(\gamma+\gamma')$ in Figs. 3(a) and 5(a). At lower temperatures, γ' -precipitates formed in the FCC- γ . The formation of phases in the investigated alloy can be mainly controlled by the solidification rate. The rodlike eutectic $(\gamma+G)$ -phase prevailed in the interdendritic regions, which should be beneficial both for strength and ductility of the alloy.

The above analysis showed that the solidification of the investigated alloy took place under non-equilibrium conditions, even during DTA, which was carried out at a cooling rate of 10 °C/min. Faster cooling rates, especially for continuous casting, caused finer microstructure and absence of the AlNi_6Si_3 phase. The appropriate chemical composition of the alloy, which is mainly determined by the sufficient fractions of Nb and Si, caused the low melting temperature, primarily due to the formation of the G -phase, and its presence in the microstructural constituents formed during the latest stages of solidification. Thus, these constituents replace (FCC- γ + NiBe) eutectic in Be-containing Ni–Cr dental alloys [6,8]. In the investigated alloy, the $(\gamma+MC)$, $(\gamma+M_3B_2)$ and $(\gamma+\text{NiBe})$ eutectics did not appear due to their very low contents.

4 Conclusions

1) The as-cast microstructure consisted of dendritic FCC- γ with precipitates $L1_2$ - γ' , G -phase ($\text{Nb}_6\text{Ni}_{16}\text{Si}_7$) and Al–Ni–Si phase (AlNi_6Si_3) in the interdendritic regions. The formation of AlNi_6Si_3 was suppressed during continuous casting.

2) A balanced addition of Si and Nb resulted in a vast solidification range, causing the formation of a low-melting (FCC- $\gamma+G$ -phase) microstructural constituent that replaced the low-melting (FCC- γ + NiBe) eutectic in the Be-bearing dental alloys.

3) The microstructure formed during continuous casting was much finer than that formed during investment casting, which resulted in very good mechanical properties (yield stress around 1000 MPa) and large ability for plastic deformation (15% at fracture).

4) The solidification sequence was described well by the Scheil solidification model. It was only unable to predict the presence of the AlNi_6Si_3 phase.

5) The investigated alloy will provide an excellent basis for further improvements in the field of dental alloys, and it may find an application in other areas due to its good mechanical properties.

Acknowledgements

This work was supported by the ARRS under the framework of the Slovenian-Brazilian Bilateral Project BI-BR/12-14-003. The TEM investigations in TU Graz have received funding from the European Union Seventh Framework Programme under Grant Agreement 312483–ESTEEM2 (Integrated Infrastructure Initiative–I3). We acknowledge Dr. Cristian Gspan for TEM-investigations.

References

- [1] WATAHA J C. Alloys for prosthodontic restorations [J]. *Journal of Prosthetic Dentistry*, 2002, 87: 351–363.
- [2] NIINOMI M, NAKAI M, HIEDA J. Development of new metallic alloys for biomedical applications [J]. *Acta Biomaterialia*, 2012, 8: 3888–3903.
- [3] BUYUKOZTURK S, GELINCIK A, UNAL D, DEMIRTURK M, CELIK D D, ERDEN S, COLAKOGLU B, KURUCA S E. Oral nickel exposure may induce type I hypersensitivity reaction in nickel-sensitized subjects [J]. *International Immunopharmacology*, 2015, 26: 92–96.
- [4] SETCOS J C, BABAEI-MAHANI A, SILVIO L D, MJÖR I A, WILSON N H F. The safety of nickel containing dental alloys [J]. *Dental Materials*, 2006, 22: 1163–1168.
- [5] ZUPANIC F, BONCINA T, KRIZMAN A, TICHELAAR F D. Structure of continuously cast Ni-based superalloy Inconel 713C [J]. *Journal of Alloys and Compounds*, 2001, 329: 290–297.
- [6] ALKMIN L B, NUNES C A, DOS SANTOS C. The development of alloys Ni–Cr for dental prosthesis [M]. Sao Paulo: University of Sao Paulo Press, 2011.
- [7] STRUPP C. Beryllium metal I. Experimental results on acute oral toxicity, local skin and eye effects, and genotoxicity [J]. *Ann Occup Hyg*, 2011, 55: 30–42.
- [8] PAN J, GEISGERSTORFER J, THIERRY D, LEYGRAF C. Electrochemical studies of the influence of beryllium on the corrosion-resistance of Ni–25Cr–10Mo cast alloys for dental application [J]. *Journal of the Electrochemical Society*, 1995, 142: 1454–1458.
- [9] ZUPANIC F, BONCINA T, KRIZMAN A, TICHELAAR F D. Microstructural evolution on continuous casting of nickel based superalloy Inconel*713C [J]. *Materials Science and Technology*, 2002, 18: 811–819.
- [10] ZUPANIC F, BONCINA T, KRIZMAN A, MARKOLI B, SPAIC S. Microstructural constituents of the Ni-based superalloy GMR 235 in the as-cast condition [J]. *Scripta Materialia*, 2002, 46: 667–672.
- [11] HOLMAN K L, MOROSAN E, CASEY P A, LI L, ONG N P, KLIMCZUK T, FELSER C, CAVA R J. Crystal structure and physical properties of $\text{Mg}_6\text{Cu}_{16}\text{Si}_7$ -type $\text{M}_6\text{Ni}_{16}\text{Si}_7$, for M = Mg, Sc, Ti, Nb, and Ta [J]. *Materials Research Bulletin*, 2008, 43: 9–15.
- [12] ALVINO A, RAMIRES D, TONTI A, LEGA D. Influence of chemical composition on microstructure and phase evolution of two HP heat resistant stainless steels after long term plant-service aging [J]. *Materials at High Temperatures*, 2014, 31: 2–11.
- [13] JAVAHERI V, SHAHRI F, MOHAMMADNEZHAD M, TAMIZIFAR M, NASERI M. The effect of Nb and Ti on structure and mechanical properties of 12Ni–25Cr–0.4C austenitic heat-resistant steel after aging at 900 °C for 1000 h [J]. *Journal of Materials Engineering and Performance*, 2014, 23: 3558–3566.
- [14] LONG Y T, NIE P L, LI Z G, HUANG J, LI X, XU X M. Segregation of niobium in laser cladding Inconel 718 superalloy [J]. *Transactions of Nonferrous Metals Society of China*, 2016, 26: 431–436.

- [15] DURAND-CHARRE M. The microstructure of superalloys [M]. Amsterdam, Netherlands: Gordon and Breach Science Publishers, 1997.
- [16] NAKAMURA T, KANENO Y, INOUE H, TAKASUGI T. The effect of second-phase Ni solid solution on environmental embrittlement of L1(2)-type Ni-3(Si,Ti) ordered alloy [J]. Materials Science and Engineering A, 2004, 383: 259–270.
- [17] MA D, SAHM P R. Single-crystal solidification of a Ni-base superalloy SRR 99. Part 3. Evolution of microstructure during directional solidification [J]. Journal of Metals Science, 1996, 87: 640–644.
- [18] ZHAO G D, YANG G L, LIU F, XIN X, SUN W R. Transformation mechanism of (γ plus γ') and the effect of cooling rate on the final solidification of U720Li alloy [J]. Acta Metallurgica Sinica, 2017, 30: 887–894.
- [19] BARAGAR D L, SAHOO M, SMITH R W. Structural modification of complex-regular eutectics of bismuth–lead, bismuth–tin and bismuth–thallium [J]. Journal of Crystal Growth, 1977, 41: 278–286.
- [20] CUI R J, HUANG Z H. Microstructural evolution and stability of second generation single crystal nickel-based superalloy DD5 [J]. Transactions of Nonferrous Metals Society of China, 2016, 26: 2079–2085.
- [21] DAVIS J R. ASM specialty handbook: Heat-resistant materials [M]. Ohio: ASM International, 1997.
- [22] PELLIZZARI M. Thermodynamic modeling for the alloy design of high speed steels and high chromium cast irons [J]. Materials and Technologies, 2010, 44: 121–127.
- [23] DI X J, CHEN B. Solidification behaviour of a high chromium nickel base alloy weld deposited metal [J]. Science and Technology of Welding and Joining, 2015, 20: 325–329.
- [24] XING X X, DI X J, WANG B S. The effect of post-weld heat treatment temperature on the microstructure of Inconel 625 deposited metal [J]. Journal of Alloys and Compounds, 2014, 593: 110–116.
- [25] MURATA Y, YUKAVA N, NODA T, MITANI T. Solidification behaviour of a nickel-base superalloy [J]. Journal of the Iron and Steel Institute of Japan, 1985, 71: 127–134.
- [26] DUPONT J N, ROBINO C V, MICHAEL J R, NOTIS M R, MARDER A R. Solidification of Nb-bearing superalloys. Part I: Reaction sequences [J]. Metallurgical and Materials Transactions A, 1998, 29: 2785–2796.
- [27] DI X J, LIU X Q, CHEN C X, WANG B S, GUO X J. Effect of post-weld heat treatment on the microstructure and corrosion resistance of deposited metal of a high-chromium nickel-based alloy [J]. Acta Metallurgica Sinica, 2016, 29: 1136–1143.

无镍基牙科合金的凝固

Franc ZUPANIČ¹, Carlos A. NUNES², Gilberto C. COELHO²,
Paula L. CURY², Gorazd LOJEN¹, Tonica BONČINA¹

1. Faculty of Mechanical Engineering, University of Maribor, 2000 Maribor, Slovenia;

2. Department of Materials Engineering, School of Engineering,
University of Sao Paulo, 12602-810 Lorena, Sao Paulo, Brazil

摘要: 通过熔模铸造和连续浇铸两种方法制备富含硅和铌、不含镍的新型镍基合金，研究合金在凝固过程中的显微组织演化及其力学性能。合金凝固开始于 FCC- γ 的结晶，随后发生二元共晶反应，形成异构组分 FCC- γ +G 相，取代含镍合金中的低熔点共晶体(FCC- γ +NiBe)。凝固末期，在熔模铸造法制备的合金中形成 AlNi₆Si₃ 和 γ' 相，而在连续浇铸法制备的合金中，AlNi₆Si₃ 相的形成受到抑制。Scheil 凝固模型与实验结果吻合较好。

关键词: 凝固；镍合金；连续浇铸；熔模铸造；显微组织；牙科合金

(Edited by Wei-ping CHEN)